AGU PUBLICATIONS

Geophysical Research Letters

RESEARCH LETTER
10.1002/2017GL074323

Key Points:
- We perform dynamic rupture simulations of the 1992 Landers earthquake with inelastic response in the fault damage zone
- Plastic yielding in fractured fault zones results in a shallow slip deficit of approximately 25-95% and off-fault deformations between approximately 20 and 90%
- Simulated off-fault deformations obtained for moderately fractured rocks are consistent with values reported from aerial image correlations

Supporting Information:
- Supporting Information S1

Correspondence to:
D. Roten,
droten@mail.sdsu.edu

Citation:
Roten, D., K. B. Olsen, and S. M. Day (2017), Off-fault deformations and shallow slip deficit from dynamic rupture simulations with fault zone plasticity, *Geophys. Res. Lett.*, *44*, 7733–7742, doi:10.1002/2017GL074323.

Received 28 MAY 2017
Accepted 13 JUL 2017
Accepted article online 18 JUL 2017
Published online 11 AUG 2017

Off-fault deformations and shallow slip deficit from dynamic rupture simulations with fault zone plasticity

D. Roten[1], K. B. Olsen[1], and S. M. Day[1]

[1]Department of Geological Sciences, San Diego State University, San Diego, California, USA

Abstract Kinematic source inversions of major ($M \geq 7$) strike-slip earthquakes show that the slip at depth exceeds surface displacements measured in the field, and it has been suggested that this shallow slip deficit (SSD) is caused by distributed plastic deformation near the surface. We perform dynamic rupture simulations of M 7.2–7.4 earthquakes in elastoplastic media and analyze the sensitivity of SSD and off-fault deformation (OFD) to rock quality parameters. While linear simulations clearly underpredict observed SSD and OFDs, nonlinear simulations for a moderately fractured fault damage zone predict a SSD of 44–53% and OFDs of 39–48%, consistent with the 30–60% SSD and 46 ± 10% (1σ) OFD reported for the 1992 M 7.3 Landers earthquake. Both SSD and OFDs are sensitive to the quality of the fractured rock mass inside the fault damage zone, and surface rupture is almost entirely suppressed in poor quality material.

1. Introduction

Coseismic surface deformations determined from geodetic observations (e.g., INSAR, differencing of Lidar or optical imaginery) indicate that the slip at depth is systematically larger than surface slip observed in the field after major ($M \geq 7$) strike-slip earthquakes [e.g., *Simons et al.*, 2002]. This shallow slip deficit (SSD) is reflected in kinematic slip inversions of geodetic data, which place the zone of highest coseismic slip at 4–6 km depth. Examples include the 1992 M 7.3 Landers earthquake [e.g., *Fialko*, 2004a], the 1999 M 7.1 Hector Mine earthquake [e.g., *Simons et al.*, 2002], the 1999 M 7.5 Izmit earthquake [*Reilinger et al.*, 2000], or the 2010 M 7.2 El-Mayor Cucapah earthquake [*Kaneko and Fialko*, 2011; *Gonzalez-Ortega et al.*, 2014]. Extreme cases of the SSD model are represented by the 2005 M 6.5 Bam [*Fialko et al.*, 2005] and the 2010 M 7.0 Haiti [*Bilham*, 2010] earthquakes, where the rupture failed to break the surface despite significant slip at shallow (4–5 km) depth.

Because surface slip measurements are central to many problems in probabilistic seismic hazard assessment, earthquake engineering, earthquake physics, and paleoseismology, it is crucial to understand the origin of the SSD. Frictional models of the seismic cycle based on a rate-and-state law [*Marone et al.*, 1991] predict a decrease of slip toward the free surface [*Scholz*, 1998], which would be consistent with the observed SSD. These rate-and-state models also imply that the deficit of slip near the surface is accommodated by afterslip or fault creep in the interseismic period [*Marone et al.*, 1991; *Rice*, 1993]. However, for the previously mentioned $M7$ strike-slip earthquakes associated with a significant SSD, afterslip or interseismic creep was either not observed or far too low to compensate for the inferred coseismic slip deficit near the surface [*Jacobs et al.*, 2002; *Fialko*, 2004b; *Fialko et al.*, 2005; *Fielding et al.*, 2009].

An alternative explanation is that the SSD is accounted for by shallow, distributed off-fault deformation. Such coseismic off-fault deformation has been documented from many recent surface-rupturing strike-slip earthquakes, such as the 1992 M 7.3 Landers earthquake [*Liu et al.*, 2003; *Milliner et al.*, 2015], the 1999 M 7.5 Izmit earthquake [*Hartleb et al.*, 2002; *Rockwell et al.*, 2002], the 1999 M 7.1 Hector Mine earthquake [*Treiman et al.*, 2002], the 2010 M 7.1 Darfield earthquake [*Van Dissen et al.*, 2011], or the 2013 M 7.7 Balochistan earthquake [*Zinke et al.*, 2014]. Geologic observations indicate that faults are often surrounded by wide zones of damaged or fractured rocks [e.g., *Sylvester*, 1988; *Rockwell and Ben-Zion*, 2007]. As seismic waves travel slower in damaged rocks than in undisturbed wall rock, these damage zones are detectable as low-rigidity zones using seismic [e.g., *Li et al.*, 1990; *Vidale and Li*, 2003; *Li et al.*, 2004] and geodetic [e.g., *Fialko et al.*, 2002; *Cochran et al.*, 2009] observations. Dynamic rupture propagation models suggest that rocks surrounding the fault fail

inelastically during earthquakes [*Yamashita*, 2000; *Andrews*, 2005; *Ben-Zion and Shi*, 2005; *Templeton and Rice*, 2008], with the permanent plastic strain forming a "flower-like" damage zone that widens dramatically near the surface [*Ma*, 2008; *Ma and Andrews*, 2010].

Although coseismic or postseismic inelastic deformation is frequently cited as explanation for the inferred shallow slip deficit [e.g., *Simons et al.*, 2002; *Fialko et al.*, 2005; *Fielding et al.*, 2009; *Dolan and Haravitch*, 2014; *Milliner et al.*, 2015], no numerical model has yet been presented which quantitatively reproduces the amount of SSD reported for major strike-slip earthquakes. The most comprehensive work in this direction was carried out by *Kaneko and Fialko* [2011] (hereafter referred to as KF11), who performed 2-D (antiplane) simulations of dynamic rupture in a homogeneous half-space. KF11 found that the amount of SSD scales with the inelastic deformation near the surface, with a maximum SSD of 15% obtained for a cohesionless crust. As these values were 2–4 times lower than the 30–60% of SSD inferred from kinematic inversions, KF11 also investigated how bias introduced by assumptions in kinematic inversions (in particular, the assumption of elastic response) would affect the inferred SSD. Nevertheless, the discrepancy between 2-D simulations and observations could not be resolved. KF11 acknowledged that the effects of 3-D geometry may be important and suspected that the amount of SSD would be higher in dynamic rupture simulations carried out for a 3-D medium.

In this study, we seek to reproduce the slip and surface deformation patterns observed during past earthquakes by running 3-D simulations of dynamic rupture in a realistic, viscoelastoplastic medium. Using the 1992 M_w7.3 Landers earthquake as a test case, we compare the SSD obtained for different rock strength models with values from source inversions and compare simulated off-fault deformation patterns with observations made from aerial image correlations [*Milliner et al.*, 2015, 2016].

2. Simulation of Dynamic Rupture With Fault Zone Plasticity

Simulations are carried out using the AWP-ODC finite difference code [*Olsen*, 1994; *Day and Bradley*, 2001; *Cui et al.*, 2010], which simulates spontaneous rupture with a traction-at-split-node method [*Dalguer and Day*, 2007] and accounts for Drucker-Prager plasticity using the return-map algorithm [*Roten et al.*, 2016]. The method has been verified against several independent finite element and finite difference codes within the Southern California Earthquake Center (SCEC) dynamic rupture code verification project [*Harris et al.*, 2009, 2011].

Effects of irregular fault geometry (correlations between fault complexity and distributed deformation were reported by *Zinke et al.* [2014] and *Milliner et al.* [2015, 2016]) and shallow velocity strengthening are likely important [KF11]. In order to assess whether the observed SSD can be explained by plasticity effects alone, we chose a simple friction law and fault geometry, thereby avoiding interplay between effects of fault roughness, rate-and-state friction and nonlinearity. Several numerical modeling studies have shown that plastic effects can be significant for these approximations [e.g., *Andrews*, 2005; *Dunham et al.*, 2011a; *Kaneko and Fialko*, 2011; *Roten et al.*, 2017].

2.1. Generation of Crustal Model

We used the SCEC (Southern California Earthquake Center) community velocity model CVM-S (version 4.26) [*Magistrale et al.*, 2000; *Lee et al.*, 2014] and the UCVM framework (Unified Community Velocity Model) [*Gill et al.*, 2013] to generate a structural model representative of the conditions within the Landers fault system. The structural model includes small-scale heterogeneities [e.g., *Savran and Olsen*, 2016] and a low-velocity zone (LVZ) around the fault (Figure S2 in the supporting information). A detailed description of the velocity model used in the simulation is provided in supporting information Text S1. The minimum shear wave velocity in our model is 200 m/s near the surface (Figure 1a). Using a resolution of 50 m, our simulation includes frequencies up to 0.8 Hz using 5 grid points per wavelength.

2.2. Definition of Initial Stress Field and Friction Parameters

In dynamic rupture simulations with off-fault inelasticity, assumptions made for the initial stress field determine normal and shear stresses on the fault, as well as the Drucker-Prager yield stress throughout the medium. The intermediate principal stress, σ_2, is taken as vertical [*Dalguer and Mai*, 2008] and computed from the lithostatic load. Effective major and minor principal stresses, σ_1' and σ_3', respectively, are assumed to be rotated by 45° with respect to the fault and computed from σ_2' using

$$\sigma_1' = 1.4\,\sigma_2' \quad \text{and} \quad \sigma_3' = 0.6\,\sigma_2'. \tag{1}$$

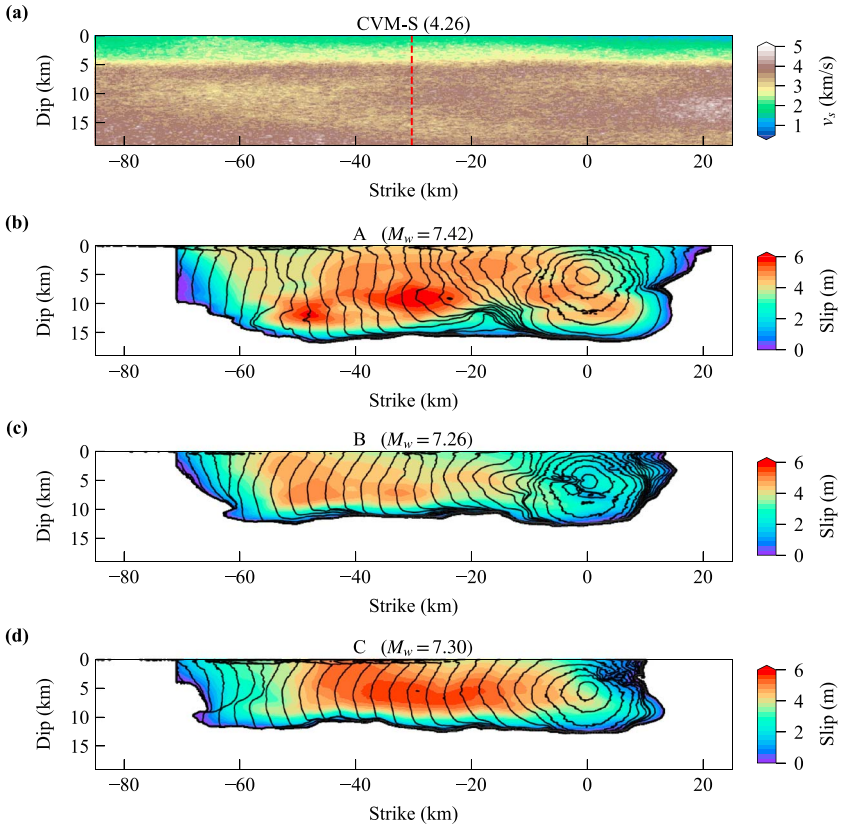

Figure 1. Fault surface used for dynamic rupture simulations showing (a) shear wave velocity and final slip obtained from rupture models (b) A, (c) B, and (d) C in the linear case. The red dashed line in Figure 1a shows the location of the cross sections shown in Figure 5. Black contours in Figures 1b–1d show rupture times in 1 s intervals.

The fault is parallel to the *x* axis in our model, with

$$\tau'_{xy} = 0.4\,\tau'_{yy} \quad \text{and} \quad \tau'_{xx} = \tau'_{yy} = \tau'_{zz}. \tag{2}$$

These values are identical to the stress field used by *Ma* [2008] and *Ma and Andrews* [2010].

We applied a von Karman autocorrelation functions to static and dynamic friction coefficients to introduce heterogeneity in the final slip of our rupture models [*Roten et al.*, 2017], with autocorrelation lengths specified according to *Mai and Beroza* [2002] (Table S1). We used average static friction coefficients between 0.525 and 0.6 and average dynamic friction coefficients between 0.3 and 0.325 (Table S1). To aid rupture propagation, the critical slip distance d_c was set to 0.6 m, slightly lower than the 0.8 m used by *Olsen et al.* [1997], *Peyrat et al.* [2001], and *Aochi and Fukuyama* [2002]. A more detailed description of rupture parameters is provided in supporting information Text S2. No attempt was made to artificially reduce slip near the surface, e.g., by increasing d_c [e.g., *Aochi and Fukuyama*, 2002; *Roten et al.*, 2011] or tapering off the shear stress [e.g., *Cui et al.*, 2010]. We assume that shallow on-fault slip is suppressed entirely by fault zone plasticity.

Source inversions performed for the Landers earthquake resolve the largest slip patch 25–40 km NW of the hypocenter, with a maximum slip of ~6 m at depth [e.g., *Cohee and Beroza*, 1994; *Freymueller et al.*, 1994; *Hernandez et al.*, 1999; *Xu et al.*, 2016]. We performed dynamic rupture simulations for many different realizations of the random field and selected three rupture models with the largest slip in the same general areas (Figures 1b–1d).

2.3. Definition of Four Rock Quality Models

The Drucker-Prager yield stress $Y(\tau)$ is expressed in terms of friction angle φ and cohesion C:

$$Y(\tau) = \max\left(0, C\cos\varphi - (\tau_m + P_f)\sin\varphi\right), \tag{3}$$

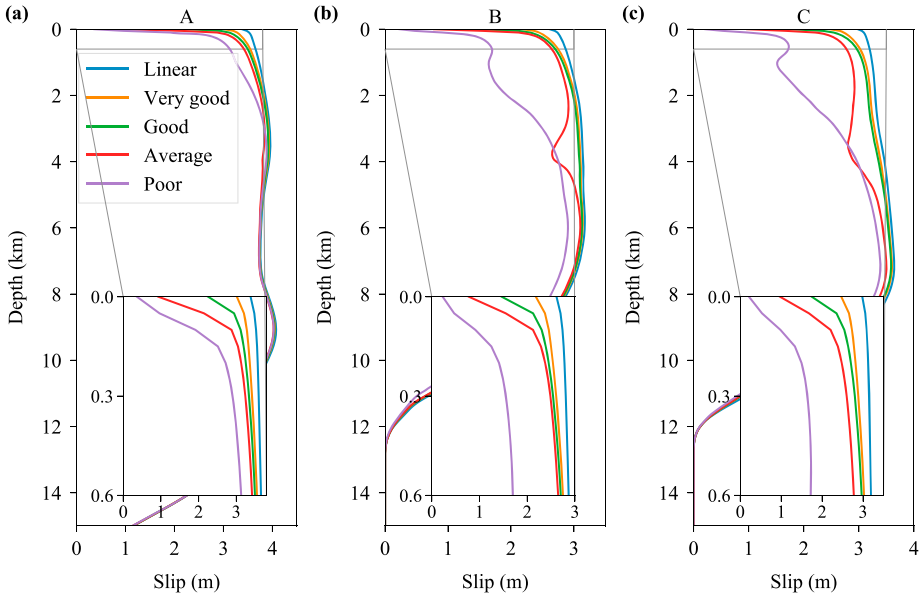

Figure 2. Mean surface slip (averaged along-strike direction) obtained for rupture models (a) A, (b) B, and (c) C in the linear case and in the nonlinear case for different rock strength parameters. The inset plot shows the mean slip near the surface.

where $\tau_m = \frac{1}{3}\left(\tau_{xx} + \tau_{yy} + \tau_{zz}\right)$ is the mean stress. The depth of the water table is taken as zero for the computation of the fluid pressure, P_f. Because small samples selected for laboratory experiments (in particular, drill cores) are typically free of preexisting cracks on which failure can occur, laboratory-determined values of φ and C do not represent the strength of a fractured rock mass [*Wyllie and Mah*, 2005], such as a damage zone surrounding a fault. The Geological Strength Index (GSI), introduced by *Hoek* [1994] and *Hoek and Brown* [1997] for mining applications, provides a system for estimating the strength of such fractured rock masses based on geological field observations. Here we use the GSI to define four rock quality models, representative of rock masses of very good, good, average, and poor quality (Table S2). The very good quality rock mass (GSI = 75) consists of well interlocked, undisturbed cubical blocks [*Hoek et al.*, 1998]. The good quality rock mass (GSI = 62.5) is already partially disturbed and contains some discontinuities. The average quality rock (GSI = 50) contains more discontinuities and is faulted or folded, while the poor quality rock (GSI = 30) is composed of poorly interlocked, heavily broken rock pieces [*Hoek et al.*, 1998]. The GSI reaches a value of 100 outside of the damage zone and at depths of more than 1 km, where the rock mass behavior approaches that of intact rock [*Marinos et al.*, 2005].

We use the Hoek-Brown failure criterion [*Hoek et al.*, 2002] to evaluate the yield surface pertaining to the chosen GSI on each node in the computational mesh [*Roten et al.*, 2017]. An equivalent friction angle and equivalent cohesion [*Hoek et al.*, 2002] is then assigned to each node, which approximates the Hoek-Brown yield surface with a DP yield surface (3). A more detailed description of the rock quality parameters is provided in the supporting information Text S3.

3. Shallow Slip Deficit From Fault Zone Plasticity

In rupture model A (M_w7.4), the peak slip exceeds 6 m at 10 km depth, with slip in excess of 4 m within a 60 km wide area (Figure 1b). Rupture model B (M_w7.26) is characterized by less slip at depth ($\leq$5 m) and near the surface. The maximum slip in rupture model C (M_w7.30) is comparable to model A but occurs closer to the surface, with surface rupture up to 5 m in the linear case (Figure 1b).

Fault zone plasticity reduces mean surface slip in rupture model A from ~3 m (linear case) to 2.5 m in very good quality rock and 2 m in good quality rock (Figure 2a). Stronger plastic effects are obtained in average and poor quality rock, with the mean surface slip dropping to 0.9 and 0.3 m, respectively. A similar behavior is observed for rupture models B and C (Figures 2b and 2c). Plastic yielding only tends to affect mean slip in the uppermost few hundreds of meters, except for the poor quality rock mass, where significant reductions of slip occur down to several km depth, especially for rupture models B and C (Figures 2b and 2c). In the absence of a

Table 1. Mean Shallow Slip Deficit (SSD, %) and Mean Off-Fault Deformation (OFD, %) $\pm 1\sigma$ Obtained From Three Dynamic Rupture Scenarios (A–C) in the Linear Case and in the Nonlinear Case Using Four Rock Strength Models[a]

			Nonlinear			
		Linear	Very Good	Good	Average	Poor
A	**SSD**	**17.3**	**25.5**	**44.2**	**76.8**	**90.9**
	OFD	8.2 ± 11.5	18.0 ± 11.5	38.8 ± 10.9	73.2 ± 12.0	88.8 ± 6.0
B	**SSD**	**17.6**	**30.5**	**53.1**	**74.9**	**92.1**
	OFD	10.0 ± 12.6	22.3 ± 9.4	48.3 ± 11.4	68.7 ± 11.3	87.3 ± 4.2
C	**SSD**	**18.1**	**31.4**	**51.2**	**72.2**	**93.7**
	OFD	9.8 ± 16.8	21.7 ± 14.0	42.2 ± 11.1	67.2 ± 11.7	81.8 ± 6.8

[a]Bold emphasizes SSD.

LVZ, the SSD is always limited to the uppermost few 100 m regardless of rock strength (Figure S5), suggesting that the depth extent of the SSD is partly controlled by the degree of fracturing in the fault damage zone.

We calculated the SSD as the ratio of the mean coseismic slip at the surface to the maximum coseismic slip (Table 1). Depth-dependent normal stress in our models results in more slip at depth than at the surface, and a SSD of 16–18%, even in the linear case. In the nonlinear case, the simulated SSD increases from 26% for very good quality rock to more than 90% in poor quality rock (Table 1). SSDs obtained for the very good and good quality rock mass are within the 30–60% range estimated for the Landers earthquake [e.g., KF11].

4. Simulated Surface Displacement

Figure 3a shows the mean fault-parallel surface displacement as function of fault distance, R_x, for rupture model E. In the linear case, the direction of the displacement changes abruptly from +1.2 m on the split node on the negative side of the fault to −1.2 m on the positive side of the fault. This behavior is very different from the pattern observed for Landers by *Milliner et al.* [2015], who correlated pairs of preevent and postevent images with the COSI-Corr (coregistration of optically sensed images and correlation) [*Leprince et al.*, 2007; *Ayoub et al.*, 2009] method to derive the near-field ground deformation with subpixel precision. The COSI-Corr derived displacement shows a gradual transition across the fault within a shear zone of finite width (Figure 3b). If fault zone plasticity is taken into account, the simulated displacement between the split nodes on adjacent

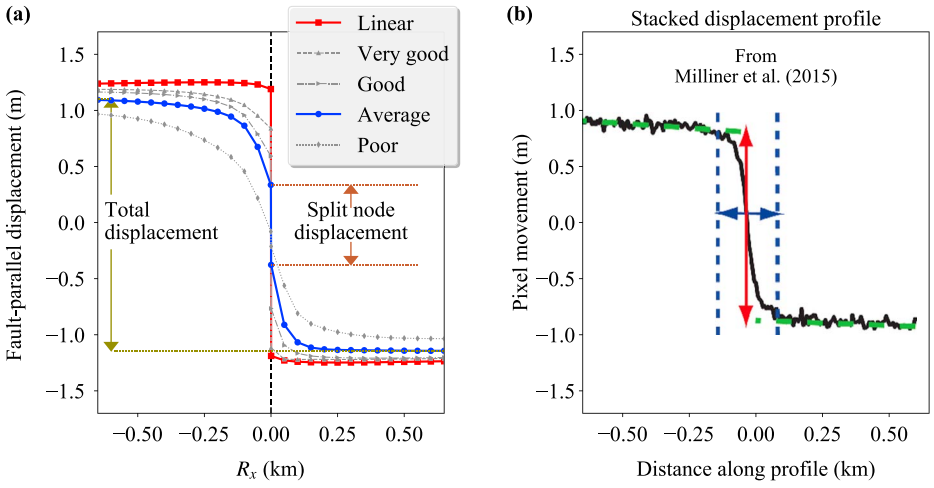

Figure 3. (a) Mean surface displacement (averaged along strike) obtained for rupture model C in the linear case and in the nonlinear case for different rock quality models. Measurements of total displacement and split node displacement are illustrated for the average quality rock model. (b) Fault-parallel displacement obtained by *Milliner et al.* [2015] from aerial image correlations along a 138 m wide profile across the Emerson Valley fault with ruptured during the M_w 7.3 Landers earthquake (modified from *Milliner et al.* [2015]). Dashed lines and arrows illustrate measurement of fault zone width.

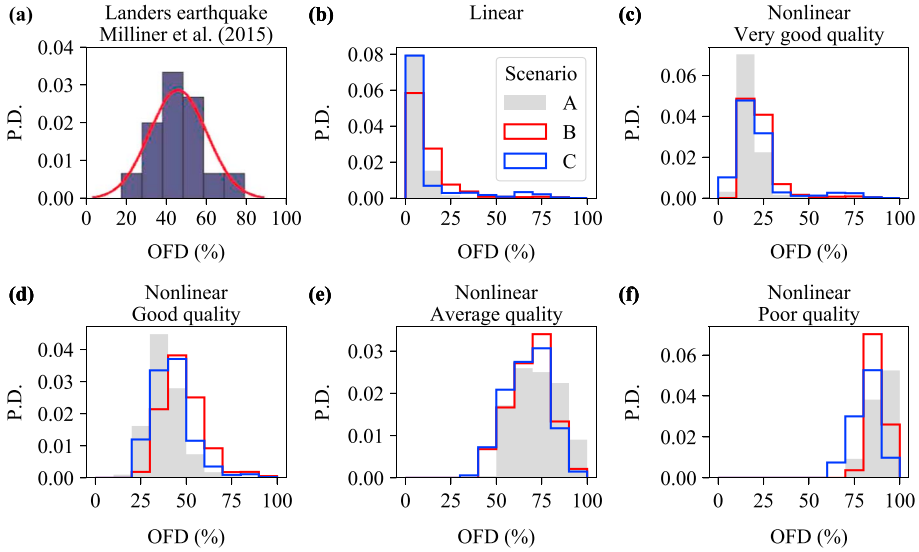

Figure 4. (a) Off-fault deformation (OFD) for Landers earthquake obtained by *Milliner et al.* [2015] from aerial image correlations (blue bars) and normal distribution with mean of 46 ± 10% (1σ, red line) (modified from *Milliner et al.* [2015]). Simulated OFD in the (b) linear case and in the nonlinear case for a rock mass of (c) very good, (d) good, (e) average, and (f) poor quality in the three rupture models. P.D. = Probability distribution.

sides of the fault decreases (Figure 3a), as more displacement is absorbed by distributed deformation near the surface.

This inelastic deformation leads to a fault zone of finite width and a smooth change in the sign of the displacement, consistent with the COSI-Corr results. The width of the shear zone increases with decreasing rock quality, and fault slip on the surface decreases, as already shown in Figure 2.

5. Off-Fault Deformation

Milliner et al. [2015] defined the relative off-fault deformation (OFD) as the difference between the total displacement measured by COSI-Corr and the displacement measured in the field [*Bryant*, 1992, 1994; *Liu et al.*, 2003], normalized by the COSI-Corr displacement. They determined the OFD for 280 cross sections and obtained a mean OFD of 46 ± 10% (1σ) following a normal distribution (Figure 4a). We compute the OFD from our simulation as the relative difference between the total displacement and the split node displacement, where the total displacement is evaluated from the maximum amount of deformation on either side of the fault (Figure 3a). The split node displacement is taken as the simulated slip between the two split nodes on adjacent sides of the fault and would correspond to the offset measured by a geologist in the field. We determined the OFD for every split node on the surface that ruptured during the simulation (split node deformation >0.1 m) and plotted the distribution (Figures 4b–4f).

OFDs obtained from linear simulations (Figure 4b) do not exceed 10% (Table 1) and exhibit a left skewed histogram that is inconsistent with the observations (Figure 4a). If plastic yielding is taken into account, OFDs increase with decreasing rock quality. Mean OFDs for good quality rock range between 38 and 48% (Table 1) in the three rupture scenarios and reproduce the observed distribution best (Figures 4a and 4d). Simulated mean OFDs for very good quality rock are lower than observed values (18–22%) and OFDs for average quality rock are higher (67–73%). In poor quality rock mean OFDs exceed 80% (Table 1) and the distribution is left skewed (Figure 4f), suggesting that this model overestimates the amount of plastic yielding that occurred during the Landers earthquake. Such poor quality rock or soil would more closely reproduce an earthquake with little or no discreet faulting but large distributed deformation, such as the 2005 *M*6.5 Bam [*Fialko et al.*, 2005] or the 2010 M_w 7.1 Darfield [*Van Dissen et al.*, 2011] earthquake.

6. Discussion and Conclusions

Three-dimensional dynamic rupture simulations with inelastic yielding in the fault zone reproduce both SSD and OFDs reported for the Landers earthquake. The degree of plastic deformation near the surface is

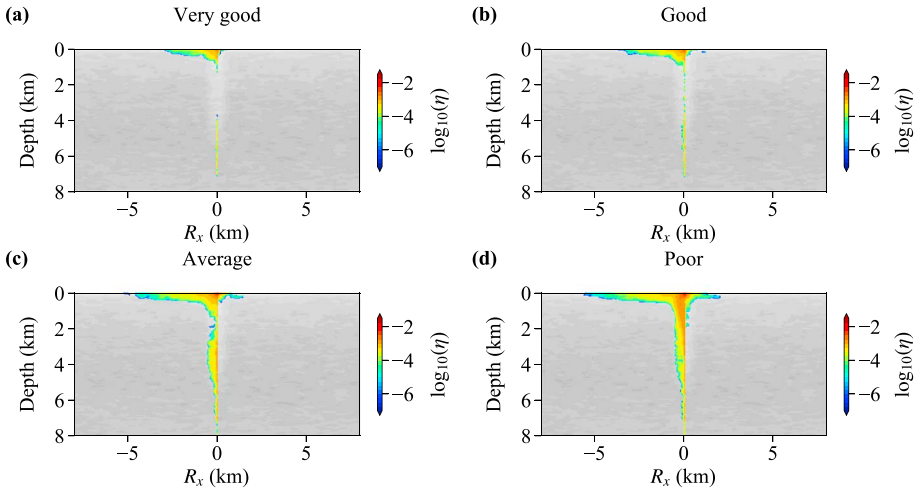

Figure 5. Distribution of plastic deformation, η, along cross sections perpendicular to fault obtained for rupture model A in (a) very good quality rock, (b) good quality rock, (c) average quality rock, and (d) poor quality rock. Gray shades reflect shear wave velocity. See Figure 1a for the location of the cross sections.

proportional to the amount of SSD (as already noted by KF11), and the mean value and distribution of OFDs. This is illustrated by the permanent plastic deformation across the fault (Figure 5), which increases with decreasing rock quality [*Ma*, 2008; *Ma and Andrews*, 2010]. All rock quality models lead to a zone of permanent plastic deformation in the uppermost few 100 m. In good and very good quality rock, plastic deformation is strongly localized and occurs only on the fault at greater depth (on-fault plasticity). In average and poor quality rock, a wide zone of permanent deformation occurs down to the maximum depth extent of the LVZ (~5 km).

Plastic yielding in the fault damage zone explains several observations made from aerial or geodetic data, including SSD, finite shear zone width, and OFD. Simulation results support the interpretation that these phenomena are caused by inelastic distributed deformation near the surface [*Simons et al.*, 2002; *Fielding et al.*, 2009; *Dolan and Haravitch*, 2014; *Milliner et al.*, 2015]. The limited depth extent of SSD produced by simulations (Figure 2) represents a remaining discrepancy with inversion results, which resolve a SSD in the top ~2 km [e.g., KF11]. Possible reasons for this discrepancy include the lack of near-surface coverage in interferometry data used for slip inversions [e.g., *Xu et al.*, 2016] or the absence of rate-and-state friction in our dynamic rupture simulations. Uncertainties related to slip inversions can be avoided by directly comparing simulated OFDs with observations (Figure 4).

The similarities between observations and simulated SSD and OFD for good quality rock (Figures 2 and 4d) suggest that this model represents the most reasonable approximation for the crystalline basement in the eastern Mojave desert. In addition, the high sensitivity of SSD and OFDs to rock quality opens the possibility to validate dynamic rupture models with fault zone plasticity against geodetic observations and to calibrate rock strength parameters from such observations for improved physics-based ground motion prediction. These results have implications for problems of seismic hazard assessment where fault zone plasticity effects are considered important, for example, critical facilities located close to an active fault [e.g. *Andrews et al.*, 2007]. Predictions of ground motions during a large ($M > 7.5$) earthquake on the southern San Andreas fault would also benefit from more accurate representations of rock strength parameters, as the intensity of simulated shaking in the Los Angeles basin is sensitive to the strength of crustal rocks [*Roten et al.*, 2014, 2017]. However, SSD and OFDs observed on the structurally immature faults that ruptured during the Landers earthquake may not be representative for mature faults, such as the San Andreas fault. *Dolan and Haravitch* [2014] suggested that the slip in structurally mature fault has progressively localized into a high-strain fault core all the way up to the surface, resulting in no distributed deformation and low shallow slip deficit. Dynamic rupture simulations with stress conditions representative of structurally mature faults capable of resolving the wavefield inside the localized high-strain fault core (width <10 m) might help explain why this is the case (Text S4).

Future simulations should also account for along-strike variations in the depth extent and width of the LVZ and along-strike variations in rock strength (where the fault intersects low strength material, such as alluvium),

as observations suggest a correlation between the type of surface lithology and the amount of deformation [*Zinke et al.*, 2014; *Milliner et al.*, 2015, 2016]. The correlation between fault zone complexity and distributed deformation found by *Milliner et al.* [2015] should be addressed using elastoplastic simulations of dynamic rupture on a more realistic representation of the Landers fault system [e.g., *Heinecke et al.*, 2014].

Acknowledgments
The authors acknowledge the Office of Science of the U.S. Department of Energy (DOE) for providing HPC resources that have contributed to the research results reported within this paper through an Innovative and Novel Computational Impact on Theory and Experiment (INCITE) program allocation award. Dynamic rupture simulations using AWP-ODC-CPU were carried out Titan, which is part of the Oak Ridge Leadership Facility at the Oak Ridge National Laboratory supported by DOE contract DE-AC05-00OR22725. The data used are listed in the references and supporting information. We thank Eric Dunham and an anonymous reviewer for valuable comments that helped to improve the manuscript. This research was supported by the Southern California Earthquake Center under SCEC award 16238. This is SCEC publication #7300.

References

Andrews, D. (1976a), Rupture propagation with finite stress in antiplane strain, *J. Geophys. Res*, *81*(20), 3575–3582.
Andrews, D. (1976b), Rupture velocity of plane strain shear cracks, *J. Geophys. Res.*, *81*(32), 5679–5687.
Andrews, D. (2005), Rupture dynamics with energy loss outside the slip zone, *J. Geophys. Res.*, *110*, B01307, doi:10.1029/2004JB003191.
Andrews, D., T. Hanks, and J. Whitney (2007), Physical limits on ground motion at Yucca Mountain, *Bull. Seismol. Soc. Am.*, *97*(6), 1771–1792.
Aochi, H., and E. Fukuyama (2002), Three-dimensional nonplanar simulation of the 1992 Landers earthquake, *J. Geophys. Res.*, *107*(B2), 2035, doi:10.1029/2000JB000061.
Ayoub, F., S. Leprince, and J.-P. Avouac (2009), Co-registration and correlation of aerial photographs for ground deformation measurements, *ISPRS J. Photogram. Remote Sens.*, *64*(6), 551–560.
Barall, M., (2010), TPV26 and TPV27 vertical fault with viscoplasticity benchmarks, Report, Invisible Software Inc., San Jose, Calif.
Baumann, C., and L. Dalguer (2014), Evaluating the compatibility of dynamic rupture-based synthetic ground motion with empirical ground-motion prediction equation, *Bull. Seismol. Soc. Am.*, *104*(2), 634–652.
Ben-Zion, Y., and Z. Shi (2005), Dynamic rupture on a material interface with spontaneous generation of plastic strain in the bulk, *Earth Planet. Sci. Lett.*, *236*(1), 486–496.
Bilham, R. (2010), Lessons from the Haiti earthquake, *Nature*, *463*(7283), 878–879.
Bizzarri, A. (2010), How to promote earthquake ruptures: Different nucleation strategies in a dynamic model with slip-weakening friction, *Bull. Seismol. Soc. Am.*, *100*(3), 923–940.
Bortugno, E. J., R. Moar, E. Taylor, and T. E. Spittler (1986), *Geologic Map of the San Bernardino Quadrangle*, Div. of Mines and Geol., Sacramento, Calif.
Bryant, W., (1992), Surface fault rupture along the Johnson Valley, Homestead Valley, and related faults associated with the M_s 7.5 28 June 1992 Landers earthquake, *Fault Eval. Rep. FER-234*, Calif. Dep. of Conserv., Div. of Mines and Geol., Sacramento, Calif.
Bryant, W., (1994), Surface fault rupture along the Homestead Valley, Emerson, and related faults associated with the M_w 7.3 28 June 1992 Landers earthquake, *Fault Eval. Rep. FER-239*, Calif. Dep. of Conserv., Div. of Mines and Geol., Sacramento, Calif.
Cochran, E. S., Y.-G. Li, P. M. Shearer, S. Barbot, Y. Fialko, and J. E. Vidale (2009), Seismic and geodetic evidence for extensive, long-lived fault damage zones, *Geology*, *37*(4), 315–318.
Cohee, B. P., and G. C. Beroza (1994), Slip distribution of the 1992 Landers earthquake and its implications for earthquake source mechanics, *Bull. Seismol. Soc. Am.*, *84*(3), 692–712.
Cui, Y., et al. (2010), Scalable earthquake simulation on petascale supercomputers, in *Proceedings of the 2010 ACM/IEEE International Conference for High Performance Computing, Networking, Storage and Analysis*, pp. 1–20, IEEE, Washington, D. C.
Dalguer, L., and S. Day (2007), Staggered-grid split-node method for spontaneous rupture simulation, *J. Geoph. Res.*, *112*, B02302, doi:10.1029/2006JB004467.
Dalguer, L., and P. Mai (2012), Prediction of near-source ground motion exceeding 1g at low frequencies ($<$ 2 Hz) from M_w ~6.5 deterministic and numerical simulations physics-based dynamic rupture simulations, in *Proceedings of 15th World Conference on Earthquake Engineering*, 10 pp., Int. Assoc. for Earthquake Eng., Lisbon, Portugal.
Dalguer, L., S. Day, K. Olsen, and V. Cruz-Atienza (2008), Rupture models and ground motion for Shakeout and other southern San Andreas fault scenarios, in *Proceedings of 14th World Conference on Earthquake Engineering*, Int. Assoc. for Earthquake Eng., Beijing, China.
Dalguer, L. A., and M. Mai (2008), Implications of style-of-faulting and loading characteristics on the dynamic rupture process, *Eos Trans. AGU*, *89*(53), S51D–1798.
Day, S., and C. Bradley (2001), Memory-efficient simulation of anelastic wave propagation, *Bull. Seismol. Soc. Am.*, *91*(3), 520–531.
Dolan, J. F., and B. D. Haravitch (2014), How well do surface slip measurements track slip at depth in large strike-slip earthquakes? The importance of fault structural maturity in controlling on-fault slip versus off-fault surface deformation, *Earth Planet. Sci. Lett.*, *388*, 38–47.
Dunham, E. M., D. Belanger, L. Cong, and J. E. Kozdon (2011a), Earthquake ruptures with strongly rate-weakening friction and off-fault plasticity, Part 1: Planar faults, *Bull. Seismol. Soc. Am.*, *101*(5), 2296–2307.
Dunham, E. M., D. Belanger, L. Cong, and J. E. Kozdon (2011b), Earthquake ruptures with strongly rate-weakening friction and off-fault plasticity, Part 2: Nonplanar faults, *Bull. Seismol. Soc. Am.*, *101*(5), 2308–2322.
Ely, G. P., T. Jordan, P. Small, and P. J. Maechling (2010), A V_{S30}-derived near-surface seismic velocity model, Abstract S51A-1907 presented at 2010 Fall Meeting, AGU, San Francisco, Calif., 13–17 Dec.
Fialko, Y. (2004a), Probing the mechanical properties of seismically active crust with space geodesy: Study of the coseismic deformation due to the 1992 M_w 7.3 Landers (southern California) earthquake, *J. Geophys. Res.*, *109*, B03307, doi:10.1029/2003JB002756.
Fialko, Y. (2004b), Evidence of fluid-filled upper crust from observations of postseismic deformation due to the 1992 M_w 7.3 Landers earthquake, *J. Geophys. Res.*, *109*, B08401, doi:10.1029/2004JB002985.
Fialko, Y., D. Sandwell, D. Agnew, M. Simons, P. Shearer, and B. Minster (2002), Deformation on nearby faults induced by the 1999 Hector Mine earthquake, *Science*, *297*(5588), 1858–1862.
Fialko, Y., D. Sandwell, M. Simons, and P. Rosen (2005), Three-dimensional deformation caused by the Bam, Iran, earthquake and the origin of shallow slip deficit, *Nature*, *435*(7040), 295–299.
Fielding, E. J., P. R. Lundgren, R. Bürgmann, and G. J. Funning (2009), Shallow fault-zone dilatancy recovery after the 2003 Bam earthquake in Iran, *Nature*, *458*(7234), 64–68.
Freymueller, J., N. King, and P. Segall (1994), The co-seismic slip distribution of the Landers earthquake, *Bull. Seismol. Soc. Am.*, *84*(3), 646–659.
Gill, D., P. Maechling, T. Jordan, A. Plesch, R. Taborda, S. Callaghan, and P. Small (2013), UCVM: An open source framework for 3D velocity model research, Abstract IN41B-1612 presented at 2013 Fall Meeting, AGU, San Francisco, Calif., 9–13 Dec.
Gonzalez-Ortega, A., Y. Fialko, D. Sandwell, F. Alejandro Nava-Pichardo, J. Fletcher, J. Gonzalez-Garcia, B. Lipovsky, M. Floyd, and G. Funning (2014), El Mayor-Cucapah (M_w 7.2) earthquake: Early near-field postseismic deformation from InSAR and GPS observations, *J. Geophys. Res. Solid Earth*, *119*, 1482–1497, doi:10.1002/2013JB010193.
Graves, R., and R. Pitarka (2016), Kinematic ground motion simulations on rough faults including effects of 3D stochastic velocity perturbations, *Bull. Seismol. Soc. Am.*, *106*(5), 2136–2153.

Harris, R., et al. (2009), The SCEC/USGS dynamic earthquake rupture code verification exercise, *Seismol. Res. Lett.*, *80*(1), 119–126.
Harris, R. A., et al. (2011), Verifying a computational method for predicting extreme ground motion, *Seismol. Res. Lett.*, *82*(5), 638–644.
Hartleb, R. D., et al. (2002), Surface rupture and slip distribution along the Karadere segment of the 17 August 1999 Izmit and the western section of the 12 November 1999 Düzce, Turkey, earthquakes, *Bull. Seism. Soc. Am.*, *92*(1), 67–78.
Heinecke, A., et al. (2014), Petascale high order dynamic rupture earthquake simulations on heterogeneous supercomputers, in *Proceedings of the International Conference for High Performance Computing, Networking, Storage and Analysis*, pp. 3–14, IEEE Press, New Orleans, La.
Hernandez, B., F. Cotton, and M. Campillo (1999), Contribution of radar interferometry to a two-step inversion of the kinematic process of the 1992 Landers earthquake, *J. Geophys. Res.*, *104*(B6), 13,083–13,099.
Hoek, E. (1994), Strength of rock and rock masses, *ISRM News J.*, *2*(2), 4–16.
Hoek, E., and E. T. Brown (1997), Practical estimates of rock mass strength, *Int. J. Rock Mech. Min. Sci.*, *34*(8), 1165–1186.
Hoek, E., P. Marinos, and M. Benissi (1998), Applicability of the Geological Strength Index (GSI) classification for very weak and sheared rock masses. The case of the Athens Schist Formation, *Bull. Eng. Geol. Environ.*, *57*(2), 151–160.
Hoek, E., C. Carranza-Torres, and B. Corkum (2002), Hoek-Brown failure criterion—2002 edition, *Proc. NARMS-Tac*, *1*, 267–273.
Jacobs, A., D. Sandwell, Y. Fialko, and L. Sichoix (2002), The 1999 (M_w 7.1) Hector Mine, California, earthquake: Near-field postseismic deformation from ERS interferometry, *Bull. Seismol. Soc. Am.*, *92*(4), 1433–1442.
Kanamori, H., H.-K. Thio, D. Dreger, E. Hauksson, and T. Heaton (1992), Initial investigation of the Landers, California, earthquake of 28 June 1992 using TERRAscope, *Geophys. Res. Lett.*, *19*(22), 2267–2270.
Kaneko, Y., and Y. Fialko (2011), Shallow slip deficit due to large strike-slip earthquakes in dynamic rupture simulations with elasto-plastic off-fault response, *Geophys. J. Int.*, *186*(3), 1389–1403.
Klimeš, L. (2002), Correlation functions of random media, *Pure Appl. Geophys.*, *159*(7-8), 1811–1831.
Lee, E.-J., P. Chen, and T. H. Jordan (2014), Testing waveform predictions of 3D velocity models against two recent Los Angeles earthquakes, *Seismol. Res. Lett.*, *85*(6), 1275–1284.
Leprince, S., F. Ayoub, Y. Klinger, and J.-P. Avouac (2007), Co-registration of optically sensed images and correlation (COSI-Corr): An operational methodology for ground deformation measurements, in *IEEE International on Geoscience and Remote Sensing Symposium (IGARSS)*, pp. 1943–1946, IEEE.
Li, Y.-G., P. Leary, K. Aki, and P. Malin (1990), Seismic trapped modes in the Oroville and San Andreas fault zones, *Science*, *249*(4970), 763–767.
Li, Y.-G., J. E. Vidale, and E. S. Cochran (2004), Low-velocity damaged structure of the San Andreas Fault at Parkfield from fault zone trapped waves, *Geophys. Res. Lett.*, *31*, L12S06, doi:10.1029/2003GL019044.
Liu, J., K. Sieh, and E. Hauksson (2003), A structural interpretation of the aftershock "Cloud" of the 1992 M_w 7.3 Landers earthquake, *Bull. Seismol. Soc. Am.*, *93*(3), 1333–1344.
Ma, S. (2008), A physical model for widespread near-surface and fault zone damage induced by earthquakes, *Geochem. Geophys. Geosyst.*, *9*, Q11009, doi:10.1029/2008GC002231.
Ma, S., and D. Andrews (2010), Inelastic off-fault response and three-dimensional dynamics of earthquake rupture on a strike-slip fault, *J. Geophys. Res.*, *115*, B04304, doi:10.1029/2009JB006382.
Magistrale, H., S. Day, R. Clayton, and R. Graves (2000), The SCEC Southern California reference three-dimensional seismic velocity model version 2, *Bull. Seismol. Soc. Am.*, *90*(6B), S65–S76.
Mai, P. M., and G. C. Beroza (2002), A spatial random field model to characterize complexity in earthquake slip, *J. Geophys. Res.*, *107*, 2308, doi:10.1029/2001JB000588.
Marinos, V., P. Marinos, and E. Hoek (2005), The geological strength index: Applications and limitations, *Bull. Eng. Geol. Environ*, *64*(1), 55–65.
Marone, C. J., C. Scholtz, and C. Bilham (1991), On the mechanics of earthquake afterslip, *J. Geophys. Res.*, *96*(B5), 8441–8452.
Milliner, C., J. Dolan, J. Hollingsworth, S. Leprince, F. Ayoub, and C. Sammis (2015), Quantifying near-field and off-fault deformation patterns of the 1992 M_w 7.3 Landers earthquake, *Geochem. Geophys. Geosyst.*, *16*(5), 1577–1598.
Milliner, C., J. Dolan, J. Hollingsworth, S. Leprince, and F. Ayoub (2016), Comparison of coseismic near-field and off-fault surface deformation patterns of the 1992 M_w 7.3 Landers and 1999 M_w 7.1 Hector mine earthquakes: Implications for controls on the distribution of surface strain, *Geophys. Res. Lett.*, *43*, 10,115–10,124, doi:10.1002/2016GL069841.
Nakata, N., and G. C. Beroza (2015), Stochastic characterization of mesoscale seismic velocity heterogeneity in Long Beach, California, *Geophys. J. Int.*, *203*(3), 2049–2054.
Olsen, K. B. (1994), Simulation of three-dimensional wave propagation in the Salt Lake basin, PhD thesis, Univ. of Utah, Salt Lake City, Utah.
Olsen, K. B., R. Madariaga, and R. J. Archuleta (1997), Three-dimensional dynamic simulation of the 1992 landers earthquake, *Science*, *278*, 834–838.
Olsen, K. B., et al. (2009), ShakeOut-D: Ground motion estimates using an ensemble of large earthquakes on the southern San Andreas fault with spontaneous rupture propagation, *Geophys. Res. Lett.*, *36*, L04303, doi:10.1029/2008GL036832.
Peyrat, S., K. Olsen, and R. Madariaga (2001), Dynamic modeling of the 1992 Landers earthquake, *J. Geophys. Res.*, *106*(B11), 26,467–26,482.
Plesch, A., et al. (2007), Community fault model (CFM) for southern California, *Bull. Seismol. Soc. Am.*, *97*(6), 1793–1802.
Reilinger, R., et al. (2000), Coseismic and postseismic fault slip for the 17 August 1999, $M=7.5$, Izmit, Turkey earthquake, *Science*, *289*(5484), 1519–1524.
Rice, J. (1993), Spatio-temporal complexity of slip on a fault, *J. Geophys. Res.*, *98*(B6), 9885–9907.
Rockwell, T. K., and Y. Ben-Zion (2007), High localization of primary slip zones in large earthquakes from paleoseismic trenches: Observations and implications for earthquake physics, *J. Geophys. Res.*, *112*, B10304, doi:10.1029/2006JB004764.
Rockwell, T. K., S. Lindvall, T. Dawson, R. Langridge, W. Lettis, and Y. Klinger (2002), Lateral offsets on surveyed cultural features resulting from the 1999 Izmit and Düzce earthquakes, Turkey, *Bull. Seismol. Soc. Am.*, *92*(1), 79–94.
Roten, D., K. B. Olsen, J. Pechmann, V. Cruz-Atienza, and H. Magistrale (2011), 3D Simulations of M 7 Earthquakes on the Wasatch fault, Utah, Part I: Long-period (0–1 Hz) ground motions, *Bull. Seismol. Soc. Am.*, *101*(5), 2045–2063.
Roten, D., K. Olsen, S. Day, Y. Cui, and D. Fäh (2014), Expected seismic shaking in Los Angeles reduced by San Andreas fault zone plasticity, *Geophys. Res. Lett.*, *41*(8), 2769–2777, doi:10.1002/2014GL059411.
Roten, D., Y. Cui, K. Olsen, S. Day, K. Withers, W. Savran, W. Peng, and D. Mu (2016), High-frequency nonlinear earthquake simulations on petascale heterogeneous supercomputers, paper presented at ACM/IEEE International Conference for High Performance Computing, Networking, Storage and Analysis (SC'16), pp. 957–968, IEEE Press, Salt Lake City, Utah, 13–18 Nov.
Roten, D., K. Olsen, Y. Cui, and S. Day (2017), Quantification of fault zone plasticity effects with spontaneous rupture simulations, *Pure Appl. Geophys.*, 1–23, doi:10.1007/s00024-017-1466-5.
Savran, W. H., and K. B. Olsen (2016), Model for small-scale crustal heterogeneity in Los Angeles basin based on inversion of sonic log data, *Geophys. J. Int.*, *205*(2), 856–863.
Scholz, C. H. (1998), Earthquakes and friction laws, *Nature*, *391*(6662), 37–42.

Shi, Z., and S. M. Day (2013), Rupture dynamics and ground motion from 3-D rough-fault simulations, *J. Geophys. Res. Solid Earth*, *118*, 1122–1141, doi:10.1002/jgrb.50094.

Sieh, K., et al. (1993), Near-field investigations of the Landers earthquake sequence, April to July 1992, *Science*, *260*, 171–171.

Simons, M., Y. Fialko, and L. Rivera (2002), Coseismic deformation from the 1999 M_w7.1 Hector Mine, California, earthquake as inferred from InSAR and GPS observations, *Bull. Seismol. Soc. Am.*, *92*(4), 1390–1402.

Sylvester, A. G. (1988), Strike-slip faults, *Geol. Soc. Am. Bull.*, *100*(11), 1666–1703.

Templeton, E., and J. Rice (2008), Off-fault plasticity and earthquake rupture dynamics: 1. dry materials or neglect of fluid pressure changes, *J. Geophys. Res.*, *113*, B09306, doi:10.1029/2007JB005529.

Treiman, J. A., K. J. Kendrick, W. A. Bryant, T. K. Rockwell, and S. F. McGill (2002), Primary surface rupture associated with the M_w7.1 16 October 1999 Hector Mine Earthquake, San Bernardino County, California, *Bull. Seismol. Soc. Am.*, *92*(4), 1171–1191.

Van Dissen, R., et al. (2011), Surface rupture displacement on the Greendale Fault during the M_w7.1 Darfield (Canterbury) earthquake, New Zealand, and its impact on man-made structures, paper presented at the Ninth Pacific Conference on Earthquake Engineering, NZSEE, Auckland, New Zealand, 14–16 Apr.

Vidale, J. E., and Y.-G. Li (2003), Damage to the shallow Landers fault from the nearby Hector Mine earthquake, *Nature*, *421*(6922), 524–526.

Wald, D. J., and T. H. Heaton (1994), Spatial and temporal distribution of slip for the 1992 Landers, California, earthquake, *Bull. Seismol. Soc. Am.*, *84*(3), 668–691.

Wills, C., and K. Clahan (2006), Developing a map of geologically defined site-condition categories for California, *Bull. Seismol. Soc. Am.*, *96*(4A), 1483–1501.

Wyllie, D., and C. Mah (2005), *Rock Slope Engineering*, CRC Press, New York.

Xu, X., X. Tong, D. T. Sandwell, C. W. Milliner, J. F. Dolan, J. Hollingsworth, S. Leprince, and F. Ayoub (2016), Refining the shallow slip deficit, *Geophys. J. Int.*, *204*(3), 1867–1886.

Yamashita, T. (2000), Generation of microcracks by dynamic shear rupture and its effects on rupture growth and elastic wave radiation, *Geophys. J. Int.*, *143*(2), 395–406.

Zinke, R., J. Hollingsworth, and J. F. Dolan (2014), Surface slip and off-fault deformation patterns in the 2013 M_w 7.7 Balochistan, Pakistan earthquake: Implications for controls on the distribution of near-surface coseismic slip, *Geochem. Geophys. Geosyst.*, *15*, 5034–5050, doi:10.1002/2014GC005538.